Dynamic light-driven metasurface: Harnessing quasibound states in the continuum for laser-induced selective crystallization

Marco Gandolfi [1,2,3] Maria Eugenia Serrano Flores [1] Jesse Frantz,[4] Jason Myers,[4] Robel Bekele,[4]
Jas Sanghera,[4] Anthony Clabeau,[5] Natalia M. Litchinitser,[6] and Maria Antonietta Vincenti [1,2,3,*]

[1]*Dipartimento di Ingegneria dell'Informazione, Università degli Studi di Brescia, Via Branze 38, 25123 Brescia, Italy*
[2]*Consiglio Nazionale delle Rircerche - Istituto Nazionale di Ottica, Via Branze 45, 25123 Brescia, Italy*
[3]*Consorzio Nazionale Interuniversitario per le Telecomunicazioni (CNIT), Viale G.P. Usberti 181/A*
Sede Scientifica di Ingegneria-Palazzina 3, 43124 Parma, Italy
[4]*US Naval Research Laboratory, 4555 Overlook Ave., SW, Washington, DC 20375, USA*
[5]*University Research Foundation, 6411 Ivy Ln. 110, Greenbelt, Maryland 20770, USA*
[6]*Department of Electrical and Computer Engineering, Duke University, Durham, North Carolina 27708, USA*

We present the design of an asymmetric metasurface made of germanium antimony tellurium nanowires that supports quasibound states in the continuum. A fully coupled optothermal model is used to show that, when exposed to brief and intense laser pulses, the metasurface undergoes a partial, geometrically controlled crystallization, thereby inducing an ultrafast dynamic wavelength shift of the quasibound state in the continuum of the order of 350 nm with pump intensities as low as 35 MW/cm^2. The proposed approach highlights the potential for controlling nanostructures' response through laser illumination, opening avenues for applications in dynamic optical modulation and beyond.

I. INTRODUCTION

Metasurfaces, characterized by their ultrathin subwavelength features designed to manipulate light at the nanoscale, have become widely used in a number of fields such as optical communication, sensing, imaging, and nonlinear optics [1–5]. Metasurfaces can be designed to support different kind of photonic resonances that are typically set at the time of fabrication. However, the same resonances can be tuned over the electromagnetic spectrum if the metasurface constituent materials are able to change their properties thanks to an external stimulus. In this context, phase change materials (PCMs) present switchable optical properties, making them excellent candidates for reprogrammable photonic circuitry [6,7].

PCMs can support structural changes of phase when properly excited through an optical, thermal, or electrical stimulus [8–13]. For example, chalcogenide-based PCMs may be used as reconfigurable devices, to serve as digital versatile disk random access memory (DVD-RAM) and Blue-ray disks [6]. $Ge_2Sb_2Te_5$ (GST from now on), is an excellent example of PCM that supports a reversible change of state between amorphous and crystalline phases. The amorphous phase can be transformed into the crystalline one when it is annealed above 150 °C and returns to the amorphous phase by a quick annealing process over 600 °C [14]. This phase transition of GST is nonvolatile [15] and, therefore, the material is stable in both phases at room temperature. GST can be crystallized and reset to the amorphous state several times, virtually without hysteresis [6,7]. On the other hand, GST possesses some volatile, intermediate crystallization states between the amorphous and crystalline phases [10,16–19]: in these intermediate states the crystallinity of GST can be controlled precisely by changing the material temperature.

The solid-state phase transition of GST comes along with a significant alteration of the optical properties, making it useful in various photonic devices. Light-induced phase transitions can be triggered by meticulously controlling optical resonances at the nanoscale: by enhancing the electric field values in small regions of space one can in fact locally increase the temperature without heating the sample by means of an external thermal source [10,16–20]. Higher resonant quality (Q) factors ensure higher field localization values and, consequently, faster phase transitions for the same amount of input laser power. Among the resonances that possess very high Q factor, quasibound states in the continuum (q-BIC) certainly stand out [21–29]. Since q-BICs have a Q factor that can be tuned almost at will and preserve the peculiar, high field localization of their dark counterparts, they lend themselves to a number of applications including sensing and nonlinear optical processes [30–34]. More specifically, it was shown that q-BIC states arising from symmetry breaking possess a Q factor that is proportional to the inverse square of the asymmetry parameter [24].

Here we demonstrate that, by leveraging the peculiar field localization provided by q-BIC modes, one can easily trigger a geometrically selective phase transition of GST in a specific portion of the metasurface. In particular, we show that a carefully designed GST metasurface can support resonant modes, which can be shifted in wavelength as much as 350 nm with

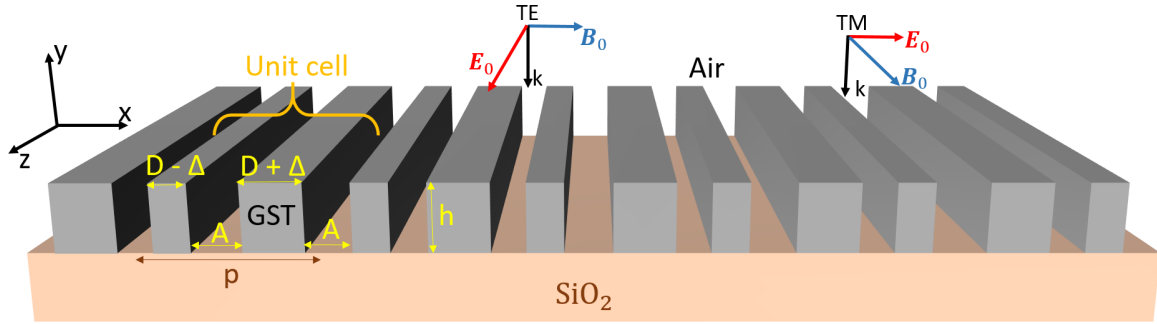*Contact author: maria.vincenti@unibs.it

FIG. 1. Sketch of the geometry considered in this work, together with the scheme of the TE and TM polarized incident plane waves.

pulse peak intensities as low as $35 \, \mathrm{MW/cm^2}$. These results will provide an effective guideline to develop novel reconfigurable photonics devices based on phase-change materials.

II. GEOMETRY AND OPTICAL MODES

The considered geometry relies on a metasurface made of GST nanowires placed over a silica substrate and immersed in air, as schematized in Fig. 1. The metasurface is periodic along the x direction with the unit cell composed of two GST nanowires of different lateral sizes and with height $h = 250$ nm. The amount of GST in the metasurface is determined by the filling ratio F and the periodicity p. These two quantities allow us to set all geometry parameters as follows: (i) the nanowires widths equal to $D = \mathrm{F} \times p/2$, (ii) the gap between the nanowires as $A = (1 - \mathrm{F})p/2$. We choose a geometry with $\mathrm{F} = 0.4$ and $p = 600$ nm, so that the gap size is $A = 180$ nm. Initially, the unit cell's nanowires are assumed to have the same width $D = 120$ nm, so that the unit cell is perfectly symmetric. In such a situation, when the GST is in the amorphous state (i.e., low temperature), the metasurface is endowed with a few symmetry-protected bound states in the continuum (BIC) modes, characterized by an infinite Q factor and, therefore, not accessible by an external radiation [26]. We refer to the Appendix B for the eigenvalue analysis of the BIC modes and their field localization profiles.

We then introduce an asymmetry in the unit cell by reducing the width of one nanowire by the quantity Δ and increasing the width of the other nanowire by the same quantity Δ. The degree of asymmetry can be quantified with the asymmetry parameter $\alpha = \Delta/D$. When the asymmetry is introduced, some of the BIC modes can evolve into q-BICs, bright modes that can interact with an external excitation [24]. Indeed, depending on the type of asymmetry that is introduced in the system, one can in turn excite only some of the modes, while keeping the others dark. Selection rules for q-BIC modes in high-contrast gratings are, in fact, related with the specific symmetry that is broken in the system [35]. All BIC modes that evolve into their leaky counterparts will still be characterized by very high, but finite, Q factors that scale as α^{-2}.

To inspect the q-BICs accessible in the geometry after performing the proposed symmetry breaking, we calculate the metasurface transmittivity upon illumination with a plane wave impinging from the air side at normal incidence. The linear response of the nanostructure is calculated by means

of rigorous coupled wave analysis (RCWA), a semianalytical method that is typically applied to solve scattering from periodic dielectric structures [36]. RCWA is a Fourier-space method, where fields are represented as a sum of spatial harmonics. It is based on the Floquet theorem stating that the solution of periodic differential equations can be expanded with Floquet functions: first, the structure is divided into uniform layers in the y direction, with each layer having its own dielectric constant. Then the electromagnetic modes in each layer are calculated and analytically propagated through the layers. Finally, the problem is solved by matching the boundary conditions at each interface between the layers using techniques such as scattering matrices. The RCWA combines well-known methods: the transfer matrix method (TMM) and the partial wave expansion method (PWEM).

In this work we always assume a very long geometry in the z direction, far exceeding the light wavelength. For this reason, the metasurface may be approximated as infinite and translationally invariant along z, hence the problem can be cast into a 2D geometry laying in the x-y plane, thus considerably reducing the numerical burden.

We consider both TE and TM polarizations for the incident light (as schematized in Fig. 1). The maps of the transmittivity as function of the asymmetry parameter α and wavelength, for both polarizations, are reported in Figs. 2(a) and 2(b), respectively. In this scenario the GST nanowires are considered at room temperature, hence in the amorphous state. The real and imaginary parts of GST dielectric permittivity are taken from Ref. [37], (the refractive index numerical values are summarized in Appendix A). As the asymmetry factor increases, narrow dips in the transmittivity spectra appear. These dips, highlighted with dashed yellow lines in Fig. 2, correspond to q-BIC modes. This is also confirmed by the fact that they become more selective and eventually disappear as α tends to zero. On the other hand, when the asymmetry becomes important (i.e., for large values of α), radiation channels open up and the q-BIC modes can be more easily excited by the external radiation, giving rise to the dips in the transmittivity spectra. In the case of TE excitation (i.e., electric field of the incident light oriented along z), two q-BICs are accessible in the near-infrared (NIR) range. We label those two q-BIC modes as the TE00 and TE01. Those two modes are located at 1608 nm and 1236 nm, respectively, when the asymmetry factor is equal to $\alpha = 0.4$. On the other hand, for TM excitation (i.e., incident electric field parallel to x), only one q-BIC mode is visible in the NIR. The latter occurs at 1212 nm for $\alpha = 0.4$
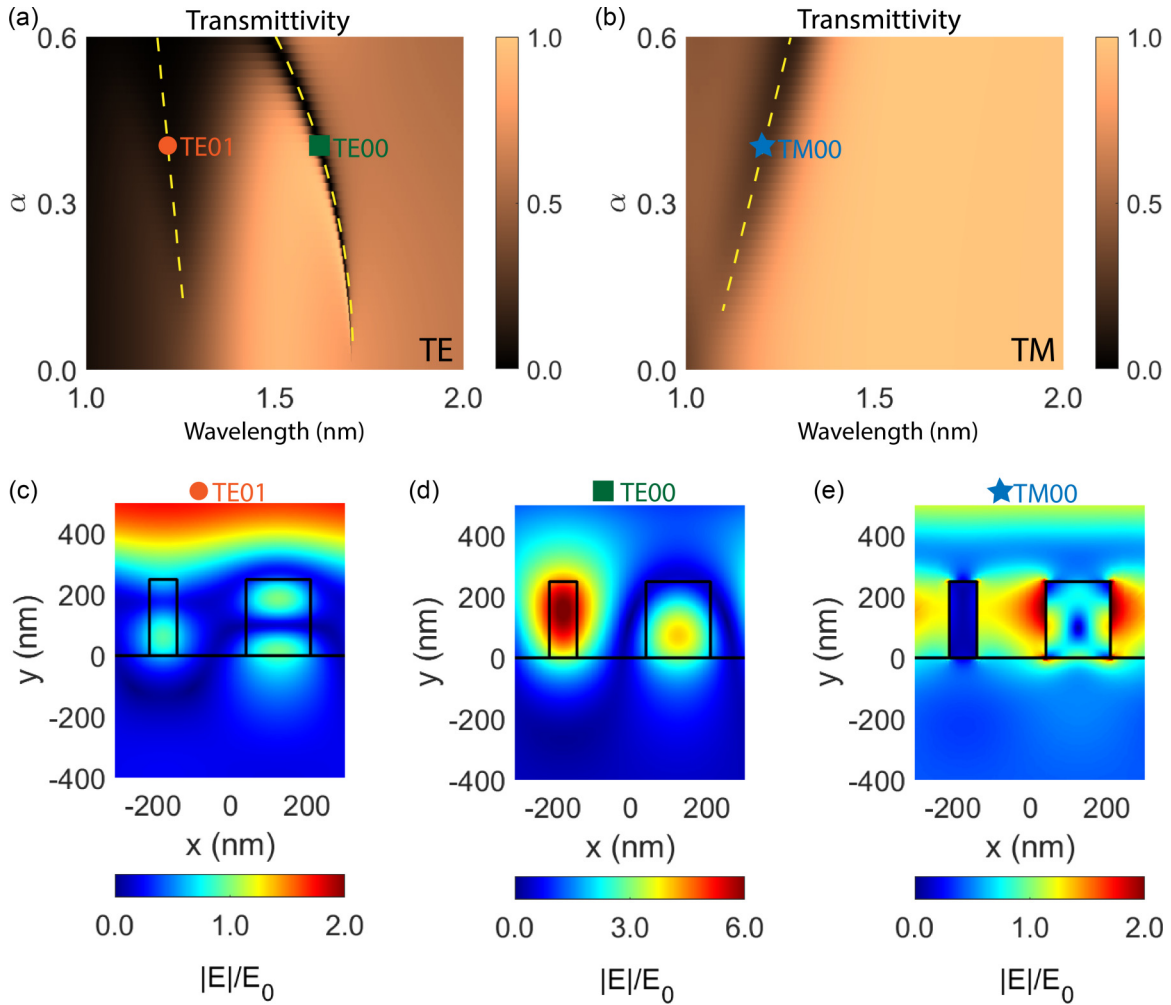
FIG. 2. (a) Transmittivity (color scale) as function of the asymmetry parameter α (vertical axis) and wavelength (horizontal axis), for TE polarized incident light (electric field oriented along z). The dashed yellow lines highlight the q-BIC modes. (b) same as (a), but for TM polarized incident light (electric field oriented along x). The electric field profiles, for the three q-BIC modes occurring when $\alpha = 0.4$ are displayed in (c)–(e). The incident plane wave, with electric field amplitude E_0, impinges from the air side at normal incidence.

and is labeled as TM00 in Fig. 2(b). We note that, while the TE00 mode in Fig. 2(a) is clearly characterized by a line width that becomes narrower as the asymmetry factor α decreases, this peculiarity is not evident for both TE01 [Fig. 2(a)] and TM00 [Fig. 2(b)]. Both modes are, in fact, barely visible in the transmittivity maps and show spectral features that are much broader than the typical q-BIC lines. We attribute this behavior to the moderate absorption of GST in the frequency range where those modes are located.

We opted to investigate the properties of a nanostructure with an asymmetry parameter $\alpha = 0.4$ that is neither too small nor too big. Very small or very large values of α will in fact present some challenges from a fabrication point of view, with the former having a value of Δ comparable with (or smaller than) the experimental tolerances and the latter yielding nanowires widths that are very small and difficult to fabricate [28]. The q-BICs occurring for $\alpha = 0.4$ are highlighted with colored markers in Figs. 2(a) and 2(b). For these three modes we evaluated the electric field distribution in the unit cell for excitation at the q-BICs wavelength by means of commercial software based on the finite elements method [38]

(implemented with COMSOL MULTIPHYSICS). The total electric field profile, normalized over the electric field amplitude of the incident plane wave, is reported in Figs. 2(c)–2(e). All q-BICs show a good degree of electric field enhancement inside and/or around the nanowires. On the other hand, we note that the identified q-BIC modes exhibit a completely different field localization profile and different field enhancement values. It is, therefore, expected that they will in turn produce different optothermal dynamics. As an example, here we delve into the light-heat dynamics triggered by the TE00 mode, which is the one that also shows the maximum field enhancement [note the different color scale ranges in Figs. 2(c)–2(e)].

III. Q-BIC MODES TIME EVOLUTION INDUCED BY A NS-PULSE

In this section we aim at studying the evolution of the crystallinity inside the GST nanowires due to the illumination with a laser pulse. For this purpose, we developed an optothermal nonlinear model implemented with COMSOL MULTIPHYSICS.

Optothermal model. The model includes an optical problem that calculates the electric field generated by the incident light. From the electric field $\mathbf{E}(\mathbf{r})$ and current density $\mathbf{J}(\mathbf{r})$ distributions it is possible to quantify the optical losses $Q_h(\mathbf{r}) = \mathrm{Re}\{\mathbf{J}(\mathbf{r}) \cdot \mathbf{E}^*(\mathbf{r})\}/2$ occurring in the GST nanowires due to light absorption. The dissipated light is converted into heat, thus triggering the thermal dynamics in the geometry, as thoroughly described in Refs. [39–41]. For this reason, a thermal problem is considered as well, in which the time-varying heat source is $g(t)Q_h(\mathbf{r})$, with $g(t) = \exp[-4\ln(2)(t - t_0)^2/\tau^2]$. In other words, the pulsed effect of the incident light is cast into the shape of the function $g(t)$ that molds the temporal dependence of the heat source. The nanostructure is illuminated by a Gaussian temporal pulse, centered at a time t_0 and with duration τ at the FWHM. Further details on the optothermal model are reported in the Appendix C.

The output of the thermal dynamics computation is useful to understand if the temperature in the nanowires exceeds the GST critical temperature $T_C \sim 150\,°\mathrm{C}$. In that case, a phase transition occurs locally, leading to an alteration of the GST complex refractive index $\tilde{n}_{\mathrm{GST}}$. However, the crystallization does not occur instantaneously, but takes some time. It is generally assumed that crystallization velocity, i.e., the velocity at which crystal growth proceeds from a nucleus upon heating an amorphous GST slab above T_C, is on the order of 1 m/s. This value has been demonstrated both theoretically [42] and experimentally [43]. Note that the magnitude of the crystallization velocity increases with temperature. However, for simplicity, we assume a fixed crystallization velocity of 1 m/s. Hence, to crystallize the nanowires of the current geometry, whose dimensions are on the scale of hundreds of nm, it takes $t_C \sim 100$ ns.

To include the crystallization dynamics in our model, we also studied the crystallinity fraction $f_C(\mathbf{r}, t)$ in the GST nanowires. $f_C(\mathbf{r}, t)$ is a positive number ranging from 0 to 1 indicating the degree of crystallinity in a certain spatial point $\mathbf{r}$ and at a time t. $f_C(\mathbf{r}, t) = 0$ if the GST is completely amorphous in a specific position $\mathbf{r}$ and at the time instant t. On the other hand, $f_C(\mathbf{r}, t) = 1$ if the GST is completely in the crystalline phase. During the phase transition, the function $f_C(\mathbf{r}, t)$ keeps track of the intermediate states between the amorphous and crystalline states, by varying continuously from 0 to 1.

To calculate $f_C(\mathbf{r}, t)$ we need to consider the thermal history at the point $\mathbf{r}$. In particular, it is reasonable to assume the following trend:

$$f_C(\mathbf{r}, t) = 1 + \left[\frac{u(\mathbf{r}, t)}{t_C} - 1\right] H\left\{1 - \frac{u(\mathbf{r}, t)}{t_C}\right\}, \qquad (1)$$

where $H\{.\}$ is the Heaviside step function, and u is a variable indicating for how much time before the instant t the temperature in the spatial point $\mathbf{r}$ has been higher than T_C. In other words, Eq. (1) assumes that $f_C(\mathbf{r}, t)$ is a piecewise function being 0 if the temperature in that spatial point has never exceeded T_C before, i.e., in that spatial point the system has never been heated up above the critical temperature, and it is, therefore, completely amorphous. On the other hand, if in $\mathbf{r}$ the temperature has been higher than T_C for a time longer than t_C, the crystallinity fraction is 1; in this case, in that spatial point the temperature exceeded T_C for a time longer than t_C,

so the system had the time to completely crystallize. In the middle situation we assume that the crystallinity fraction increases linearly from 0 to 1, proportionally with the time interval u for which $T(\mathbf{r}) > T_C$; in such a case the crystallization is only partial and increases linearly with u.

The time interval u is calculated by solving the following partial differential equation coupled with the optical and thermal problems:

$$\frac{\partial u(\mathbf{r}, t)}{\partial t} = H\left\{\frac{T(\mathbf{r}) - T_C}{1[K]}\right\}, \qquad (2)$$

solved for the nanowires only, with the initial condition $u(\mathbf{r}, t = 0) = 0$ everywhere. In other words, Eq. (2) implies that for the time instants such that $T < T_C$ the variable u is not incremented, since the right-hand side of Eq. (2) is 0. On the other hand, when $T > T_C$ the right-hand side of Eq. (2) is 1 and u increases linearly with the time interval for which the temperature exceeds T_C.

Once the temperature value has been used to compute u and in turn f_C, it is possible to update the GST refractive index $\tilde{n}_{\mathrm{GST}}$ by exploiting the effective medium approximation (EMA), i.e., $\tilde{n}_{\mathrm{GST}}(\mathbf{r}, t) = f_C(\mathbf{r}, t)\tilde{n}_C + [1 - f_C(\mathbf{r}, t)]\tilde{n}_A$, where $\tilde{n}_C$ and $\tilde{n}_A$ are the complex GST refractive index in the crystalline (high-temperature) and amorphous (low-temperature) phase, respectively (we refer to Appendix A for further comments on the EMA validity). The transiently modified GST refractive index alters the optical response at the pump, and hence the optical problem is solved again, yielding a heat source variation.

This fully coupled model therefore solves the optical, the thermal, and the crystallinity fraction problems together at the same time, in a self-consistent way, and provides a full picture of the optical and thermal dynamics occurring in the nanostructure. We point out that, for the sake of modeling, the optical problem is solved and updated for every time step. The conversion of the optical energy into heat occurs only for the duration of the pulse. However, the solution of the optical problem calculated at other time instants is useful to better appreciate the temporal evolution of the optical modes. In other words, the optical problem has a twofold applications: on one hand, it allows us to model the pump heating the system, on the other hand it serves as a probe to follow the electric field profile evolution at the q-BIC light wavelength (1608 nm, for $\alpha = 0.4$). Therefore, in our model the solution of the optical problem outside the pulse duration does not alter the thermal and phase transition dynamics.

Optothermal dynamics and transient phase transition. As one can easily infer from the field localization profiles, the thermal dynamics associated with each q-BIC mode could vary substantially. As a paradigmatic case study, here we consider the thermal dynamics of the metasurfaces with $\alpha = 0.4$ generated by a light pulse with wavelength tuned at the TE00 q-BIC, i.e., $\lambda = 1608$ nm. At the initial time of the simulation ($t = 0$), the system is at equilibrium at room temperature $T_{\mathrm{amb}} = 20\,°\mathrm{C}$. The real and imaginary parts of the refractive index in the GST nanowires are spatially homogeneous and equal to 4.03 and 9×10^{-4}, respectively, for the considered light wavelength. The situation is represented in the first line of Fig. 3.
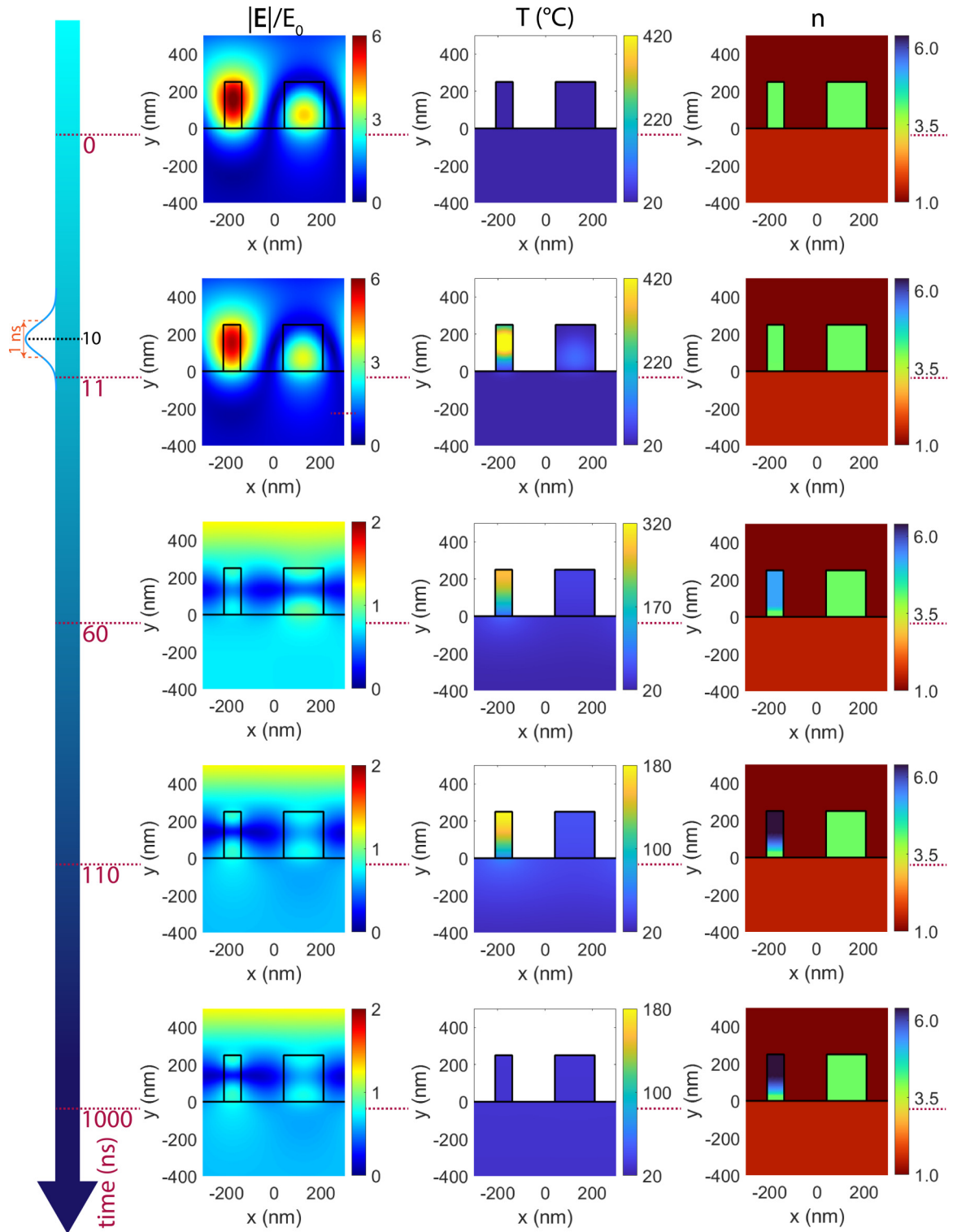
FIG. 3. Plot of the normalized electric field (left column), temperature (center column), and refractive index (right column) distributions in the metasurface unit cell. The dynamics can be appreciated by looking at the panels from top to bottom, i.e., for increasing time. The electric field and temperature color bar limits vary from one panel to the other to better highlight the spatial variations. The impinging light wavelength is set at the TE00 q-BIC mode wavelength (i.e., 1608 nm, for $\alpha = 0.4$). The peak intensity and the FWHM temporal duration of the pulse are $35.7\,\mathrm{MW/cm^2}$ and 1 ns, respectively (corresponding to a light fluence of $38\,\mathrm{mJ/cm^2}$). The light pulse illuminates the metasurface 10 ns after the initial time ($t = 0$), as indicated on the time line reported on the left of the figure.

After 10 ns the metasurface is excited with an intense pulse of duration $\tau = 1$ ns at FWHM. Optical losses occur in the GST nanowires, hence an important heat source is present in the regions of strong electric field enhancement. Such condition occurs in two regions: (i) in the lower part of the large nanowire and (ii) in the top part of the small nanowire (see Fig. 3, top left panel). However, the thermal dynamics running in these two regions is completely different. Indeed, the region with a strong heat source in the large nanowire is very close to the substrate, and the contact surface between the nanowire and the substrate is quite large. As a consequence, we expect that the substrate acts as a thermal bath with very efficient heat dissipation, thus resulting in a very small temperature increase in the large nanowire. On the other hand, a completely different situation occurs in the small nanowire. Here, the heat source is located on the top of the nanowire and the lower part of the nanowire plays the role of an impedance for the heat to flow towards the substrate. Since the width of the nanowire is small, its lower part exacerbates the resistance it plays against the heat dissipation toward the substrate. For this reason, the heat dissipation from the nanowire's top part is not very efficient and a substantial temperature increase is expected in the region of strong optical power dissipation. All these observations are substantiated in the temperature profile observed just after the end of the pulse ($t = 11$ ns). Indeed, in Fig. 3 (second line, center panel) we see that the temperature reaches a very high value only on the top part of the smaller nanowire.

The simulation displayed in Fig. 3 considers peak intensity of ~35.7 MW/cm^2 during the pulse. In this case, the maximum temperature observed in the geometry at the end of the pulse well exceeds the GST critical temperature, thus starting the crystallization process. As we have mentioned previously, the crystallization is not an instantaneous process, but it rather takes some time. Hence, after the end of the pulse the GST nanowires are still in the amorphous state, as we can see from the value of the refractive index, that is still 4.03 in all the nanowires (Fig. 3, second line, right panel).

As time passes, while the heat diffusion takes place, the crystallization in the small nanowire occurs. In particular, at $t = 60$ ns the temperature in the top part of that nanowire has become rather homogeneous, and it has exceeded T_C for almost 40–50 ns. For this reason, in the top part of the small nanowire there has been a partial crystallization, and the refractive index has increased to 5, as displayed in the third line of Fig. 3. Accordingly, the quasi-BIC mode has disappeared and the electric field distribution has changed (see Fig. 3, third line, left panel).

At $t = 110$ ns the cooling of the GST nanowires is already important, and the temperature in the top portion of the small nanowire has lowered to 180 °C, yet a value above T_C (see Fig. 3, fourth line, center panel). This means that the top part of that nanowire experienced a temperature exceeding T_C for more than 100 ns, and the complete crystallization has occurred. Therefore, the refractive index on the top part of the small nanowire equals the value of the crystalline GST, i.e., 6.44 (as displayed in Fig. 3, fourth line, right panel). Furthermore, towards the bottom of the small nanowire there is a transition region with refractive index in between the amorphous and crystalline phase (cyan color in the small nanowire
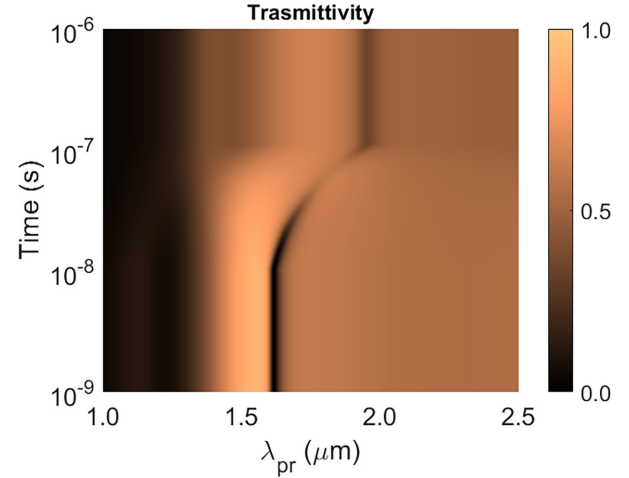

FIG. 4. Map of the transmittivity (color scale) vs time (left axis, log scale) and probe wavelength (horizontal axis). The peak intensity and the FWHM temporal duration of the pulse are 35.7 MW/cm^2 and 1 ns, respectively.

in the right panel of the fourth line). In this region there has been only a partial crystallization: this occurs because the electric field enhancement due to the pulse was not very high, and the pulse was not powerful enough to reach a temperature exceeding T_C. However, at later times the heat diffusion from the top part allowed to have a temperature increase above T_C, lasting until the cooling had not taken over. For this reason, here $T > T_C$ for a time shorter than t_C, so the crystallization was only partial.

At later times, the cooling continues and the temperature soon becomes lower than T_C. This means that the crystallization does not continue and the crystallinity degree recorded at time $t = 110$ ns does not change anymore. In particular, in the last line of Fig. 3 we display the situation after 1 µs, in which the room temperature is recovered (center panel), and the refractive index distribution is almost unchanged with respect to the right panel of the fourth line. As we can see from the left panel, due to the induced crystallinity the quasi-BIC mode at the original pump wavelength is lost, and the electric field distribution is heavily altered with respect to the initial situation.

q-BIC transient shifting. We have seen that when a portion of the GST nanowires has been crystallized the TE00 q-BIC at 1608 nm cannot be identified in the nanostructure anymore.

To understand if the q-BIC has been quenched or shifted to a different wavelength, we introduce another optical step in the fully coupled time-dependent model, to serve as a probe. The new optical step takes as an input the space-dependent refractive index in the nanowires, obtained considering the thermally induced local crystallization in the GST. In other words, for every time instant considered in the optothermal computation, we solve a new optical problem, with a space-dependent spatial distribution of the refractive index pertaining to that specific time instant. In the probe optical step, for every considered time instant, the wavelength is swept over the range 1–2.5 µm, and the metasurface's transmittivity is recorded. In Fig. 4 we report the transmittivity as function of time and probe wavelength λ_{pr}. The map shows

that before the pulse arrives ($t < 10$ ns) there is a dip in the transmittivity around 1608 nm that corresponds to the TE00 q-BIC. At 10 ns the pulse arrives and the crystallization process starts. As we have seen in Fig. 3, the refractive index in the top part of the small nanowire changes, thus resulting in a red shift of the transmittivity dip, visible in the time interval 10–100 ns in Fig. 4. Furthermore, the transmittivity dip becomes less deep.

The cooling process, on the other hand, takes over after 100 ns, hence the crystallization process stops at this time. For this reason, for longer times the dip's position does not change and occurs at the wavelength $\lambda_{pr} \sim 1.96$ µm. We can, therefore, conclude that the effect of the geometrically selective, partial crystallization occurring in the nanowires results into a shift of the q-BIC to another wavelength. For the specific pulse duration used for this analysis the q-BIC shift occurs on the time scale of 100 ns. So, the q-BIC shifting rate S, defined as the wavelength shift divided by the corresponding time interval, is ~ 3.52 nm/ns. We also stress that different pulse durations or intensities could lead to different optothermal dynamics and produce a less or more significant spectral shift.

Finally, we would like to point out that it is not possible to revert the nanowires back to the initial state with a second, intense pulse. Indeed, if the metasurface is illuminated again with a sufficiently high pump irradiance so that the reset temperature ($\sim 600\,°C$) is reached, the amorphous state is transiently recovered again. However, the complete cooling takes almost 1 µs (as highlighted in Fig. 3), so some portions of the nanowires stay at a temperature between the reset temperature ($\sim 600\,°C$) and the crystallization temperature ($\sim 150°C$) for a time span far exceeding the set time $t_C \sim 100$ ns. This paves the way for a parasite partial recrystallization during the cooling.

IV. CONCLUSIONS

A fully coupled optothermal model has been used to reveal how to exploit q-BIC modes to obtain a geometrically selective, ultrafast phase-change transition. More specifically, we demonstrated that a full crystallization of a small portion of the proposed metasurface is able to produce a controlled resonance shift as large as 350 nm. Such spectral shift occurs on the 100 ns scale and with pump intensity as low as 35 MW/cm^2. The proposed analysis lets us also envision how different modes with different field localization profiles and enhancements will lead to different crystallization profiles and, therefore, different spectral shifts and time-scale dynamics, effectively providing an advanced approach for ultrafast resonance tuning at the nanoscale level.
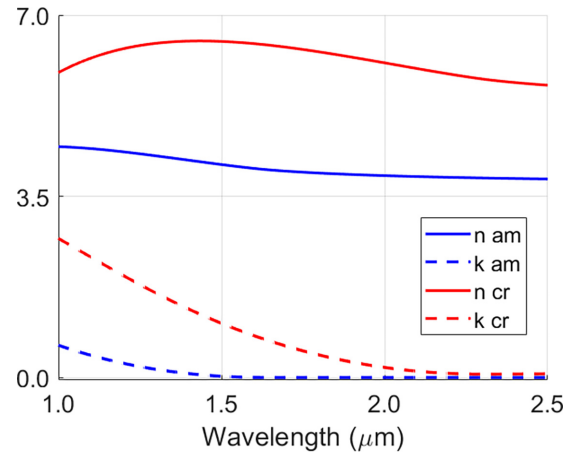
FIG. 5. Plot of the GST refractive index for the amorphous and crystalline states (blue and red lines, respectively) vs wavelength. The full (dashed) lines correspond to the refractive index real part n (to the imaginary part k).

APPENDIX A: GST REFRACTIVE INDEX

In Fig. 5 we report the refractive index for both phases of GST, taken from Ref. [37]. In particular, at the wavelength of the TE00 q-BIC for $\alpha = 0.4$ (i.e., at $\lambda = 1608$ nm), the amorphous (crystalline) state refractive index is $\tilde{n}_A = 4.03 + i9 \times 10^{-4}$ ($\tilde{n}_C = 6.44 + i0.79$).

As for the refractive index in the intermediate crystalline states, in this paper we adopt the linear effective medium approximation (EMA). In our previous publication [37] we have measured the bulk GST refractive index with ellipsometry as a function of temperature and verified, with multiple fitting attempts, that the value of the dielectric permittivity can be represented with different EMA models. For consistency with Ref. [37] here we use the linear EMA, rather than the Bruggeman method, as a fast and simple method to interpolate between crystal states' refractive index to determine the optical constants of partially crystallized films.

APPENDIX B: EIGENMODE ANALYSIS

We introduce an eigenmode analysis to address what are the optical modes available in the perfectly symmetric structure (BIC modes). The problem is solved numerically with COMSOL MULTIPHYSICS. The eigenmode analysis performed on the perfectly symmetric unit cell (i.e., for $\alpha = 0$) reveals that five modes with singular Q factor are available in the wavelength range 1.0–2.5 µm. These modes, whose electric and magnetic field profiles are shown in Fig. 6, correspond to BICs.

We track the wavelength and Q-factor evolution of the modes, as a function of the asymmetry parameter (Figs. 7 and 8, respectively). In particular, as we can see from Fig. 6, the field of the modes TE10 and TM10 is mainly concentrated in the air. Hence, the symmetry breaking involving the nanowires dimensions do not affect the Q factor of these modes, which remains infinite upon variation of α (see Fig. 8). Note that an infinite Q factor cannot be achieved with simulations, due to numerical reasons. So, a Q factor exceeding 10^8 can be
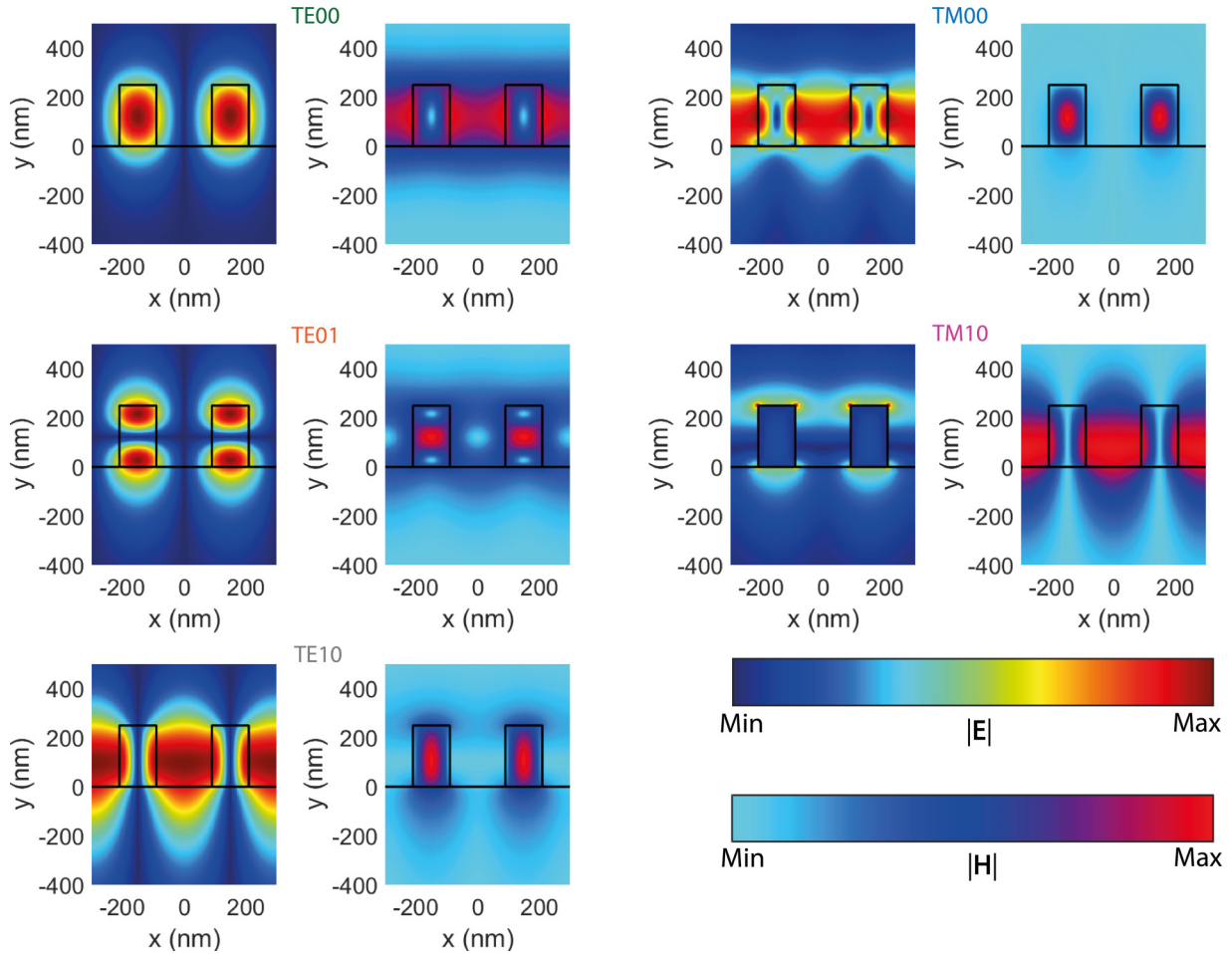
FIG. 6. Mode profile (electric and magnetic field norm, left and right panels, respectively) of the 5 BICs supported by the nanowires with $\alpha = 0$.

ascribed to a perfect BIC. For the same reason, the TE10 and TM10 Q factor small oscillations appearing in Fig. 8 are a numerical artifact.

On the other hand, the field of TE00, TE01, and TM00 modes is mainly confined within the nanowires. As a

consequence, as we introduce the asymmetry, these modes become leaky and transition into the q-BICs observed in Figs. 2(c)–2(e). The evolution of the mode wavelength as a function of the asymmetry parameter α (see Fig. 7) shows a trend compatible with the transmittivity dips appearing in
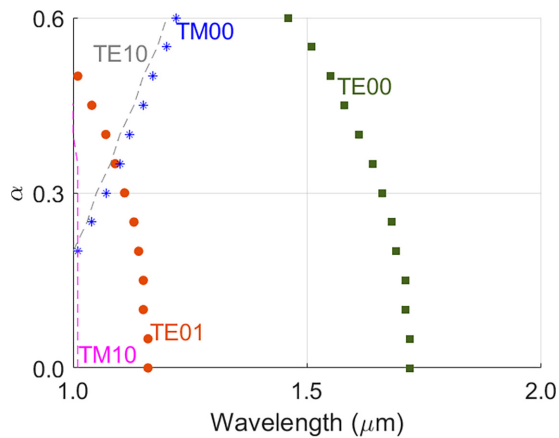

FIG. 7. Plot of the wavelength of the modes (horizontal axis), calculated with the eigenmode analysis, vs asymmetry parameter (vertical axis).
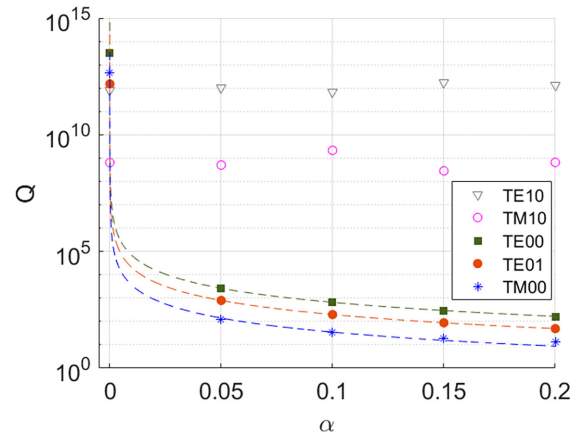

FIG. 8. Plot of the modes Q factor (vertical axis), calculated with the eigenmode analysis, vs asymmetry parameter (horizontal axis). The dashed lines are the best fit with the function $C\alpha^{-2}$.

Fig. 2(a) and 2(b). Hence, the latter dips can be safely ascribed to the metasurface q-BICs. We observe that the quality factor of the TE00, TE01, and TM00 modes scales as α^{-2} (see Fig. 8) as predicted in Ref. [24].

We point out that the results discussed in Figs. 6–8 are obtained neglecting the GST absorption coefficient, for the sake of better recognizing the q-BIC modes. However, since the absorption coefficient in the amorphous phase is quite small (see Fig. 5), the same trend is expected also for the more realistic scenario, in which the GST absorption is considered.

APPENDIX C: OPTOTHERMAL MODEL DESCRIPTION

The optothermal model considers a 2D geometry (*x*-*y* plane). The problem is solved for one unit cell of the metasurface, containing two GST nanowires. On the sides parallel to the *y* direction periodic boundary conditions are imposed.

To simulate the dynamics induced by the pump pulse we use a frequency-transient study, the frequency domain pertaining to the optics, while the time domain concerning the thermic model and the partial differential equation for the variable *u*. To simulate the probe we use a frequency domain study.

Optical problem: Further details. The air domain is truncated with a port boundary condition placed on the corresponding boundary (parallel to the *x* direction), introducing a plane wave into the simulation cell. Analogously, also the substrate domain is truncated with a port that absorbs the incoming power but does not add any plane wave excitation. The air and substrate domains heights for the optical problem are 700 and 500 nm, respectively. The refractive index of the air domain is 1, whereas the refractive index of the silica substrate is 1.45. The refractive index in the nanowires is derived from the GST refractive index reported in Appendix A. We solve the Maxwell's equations with a frequency domain approach, encompassed in the frequency-transient study (pump) or frequency domain study (probe).

Thermal problem: Further details. We calculate the temperature distribution in the nanowires and in the substrate only. Indeed, it is well known that the thermal conductivity of the air is poor, of the order of (or lower than) 10^{-2} W m^{-1} K^{-1}. As a consequence, since the external surface of our geometry is small, we expect that the main dissipation channel is the heat conduction towards the substrate. For this reason, we do not solve the thermal problem in the air domain, thus considerably reducing the burden and time of the computation. Instead, on the external boundaries where the air should be present, we assign adiabatic boundary conditions.

For the sake of completeness we have also verified that the latter assumption is correct. To this purpose, for a few case studies we have solved the problem including the air domain in the thermics as well, and temperature variations below 1 K

TABLE I. List of the parameters used in the thermal simulation.

	GST	SiO$_2$
Thermal conductivity (W m^{-1} K^{-1})	0.5 [44]	0.8
Mass density (kg m^{-3})	6200 [44]	2200
Specific Heat per unit mass (J kg^{-1} K^{-1})	240 [45,46]	800

were observed with respect to the adiabatic boundary condition case. The same result is obtained upon substitution of the adiabatic boundary conditions with convective and radiative ones on the interface where air should be present.

For the thermal simulation, the substrate height is set to 8 μm. In this way, for all the simulated time instants the heat flux and the temperature increase do not reach the lower boundary of the substrate. Hence, the particular choice of the substrate height and of the lower boundary condition does not influence the result of the thermal problem.

The temperature distribution is obtained by solving the thermal diffusion equation. The heat source $g(t)Q_h(\mathbf{r})$ is assigned in the nanowires.

We use a time-dependent approach, encompassed in the frequency-transient study. The simulated temporal span covers several temporal decades. Hence, the time step of the solution has been varied in order to obtain a precise solution within a reasonable computational time. Hence, the time step has been taken very small during the pulse duration, i.e., $\tau/10$, and later it has been progressively released to solve 100 time instants within each temporal decade. The used thermal parameters are summarized in Table I.

Estimate of the GST nanowires thermal expansion. The results presented in the main text are obtained neglecting the GST nanowires thermal expansion. Such assumption can be justified by estimating an upper limit for the GST nanowires thermal expansion.

In steady-state thermal situations, the height increase of the GST nanowires Δh follows the relation: $\Delta h/h = \alpha_T(T - T_{\mathrm{amb}})$, where α_T is the thermal expansion coefficient. For GST, $\alpha_T < 2 \times 10^{-5}$ K^{-1} [44]. The temperature increase in our simulations never exceeds 400 K, as a consequence it is straightforward to prove that the height increase Δh is smaller than 2 nm. Finally, we point out that the latter estimate considers a steady-state situation, i.e., when the temperature increase holds for a very long time. At variance, in our model we deal with a much faster thermal dynamics, further reducing the estimation for the thermal expansion value. For these reasons, the nanowires thermal expansion can be quantified to be of the order of (or smaller than) 1 nm, and therefore negligible with respect to the geometrical parameters at play.

[1] N. Yu and F. Capasso, Nature Mater. **13**, 139 (2014).

[2] A. V. Kildishev, A. Boltasseva, and V. M. Shalaev, Science **339**, 1232009 (2013).

[3] P. Genevet, F. Capasso, F. Aieta, M. Khorasaninejad, and R. Devlin, Optica **4**, 139 (2017).

[4] A. Arbabi, Y. Horie, M. Bagheri, and A. Faraon, Nature Nanotechnol. **10**, 937 (2015).

[5] S. Kruk and Y. Kivshar, ACS Photon. **4**, 2638 (2017).

[6] T. Cao, R. Wang, R. E. Simpson, and G. Li, Prog. Quantum Electron. **74**, 100299 (2020).

[7] Z. Gong, F. Yang, L. Wang, R. Chen, J. Wu, C. P. Grigoropoulos, and J. Yao, J. Appl. Phys. **129**, 030902 (2021).

[8] S. R. Ovshinsky, Phys. Rev. Lett. **21**, 1450 (1968).

[9] M. Wuttig, H. Bhaskaran, and T. Taubner, Nature Photon. **11**, 465 (2017).

[10] D.-Q. Zhang, F.-Z. Shu, Z.-W. Jiao, and H.-W. Wu, Opt. Express **29**, 7494 (2021).

[11] B. Li, R. Camacho-Morales, N. Li, A. Tognazzi, M. Gandolfi, D. de Ceglia, C. De Angelis, A. A. Sukhorukov, and D. N. Neshev, Photon. Res. **11**, B40 (2023).

[12] Q. Wang, E. T. Rogers, B. Gholipour, C.-M. Wang, G. Yuan, J. Teng, and N. I. Zheludev, Nature Photon. **10**, 60 (2016).

[13] Y.-S. Lin and Z. Xu, Int. J. Optomech. **14**, 78 (2020).

[14] K.-K. Du, Q. Li, Y.-B. Lyu, J.-C. Ding, Y. Lu, Z.-Y. Cheng, and M. Qiu, Light Sci. Appl. **6**, e16194 (2017).

[15] A. Karvounis, B. Gholipour, K. F. MacDonald, and N. I. Zheludev, Appl. Phys. Lett. **109**, 051103 (2016).

[16] F. Zhang, X. Xie, M. Pu, Y. Guo, X. Ma, X. Li, J. Luo, Q. He, H. Yu, and X. Luo, Adv. Mater. **32**, 1908194 (2020).

[17] J. Tian, H. Luo, Y. Yang, F. Ding, Y. Qu, D. Zhao, M. Qiu, and S. I. Bozhevolnyi, Nature Commun. **10**, 396 (2019).

[18] C. R. de Galarreta, I. Sinev, A. M. Alexeev, P. Trofimov, K. Ladutenko, S. G.-C. Carrillo, E. Gemo, A. Baldycheva, J. Bertolotti, and C. D. Wright, Optica **7**, 476 (2020).

[19] A. Leitis, A. Heßler, S. Wahl, M. Wuttig, T. Taubner, A. Tittl, and H. Altug, Adv. Funct. Mater. **30**, 1910259 (2020).

[20] B. Gholipour, J. Zhang, K. F. MacDonald, D. W. Hewak, and N. I. Zheludev, Adv. Mater. **25**, 3050 (2013).

[21] C. W. Hsu, B. Zhen, A. D. Stone, J. D. Joannopoulos, and M. Soljačić, Nature Rev. Mater. **1**, 16048 (2016).

[22] S. Joseph, S. Pandey, S. Sarkar, and J. Joseph, NanoPhoton. **10**, 4175 (2021).

[23] I. S. Sinev, K. Koshelev, Z. Liu, A. Rudenko, K. Ladutenko, A. Shcherbakov, Z. Sadrieva, M. Baranov, T. Itina, J. Liu *et al.*, Nano Lett. **21**, 8848 (2021).

[24] K. Koshelev, Y. Tang, K. Li, D.-Y. Choi, G. Li, and Y. Kivshar, ACS Photon. **6**, 1639 (2019).

[25] G. Zograf, K. Koshelev, A. Zalogina, V. Korolev, R. Hollinger, D.-Y. Choi, M. Zuerch, C. Spielmann, B. Luther-Davies, D. Kartashov *et al.*, ACS Photon. **9**, 567 (2022).

[26] K. Koshelev, S. Lepeshov, M. Liu, A. Bogdanov, and Y. Kivshar, Phys. Rev. Lett. **121**, 193903 (2018).

[27] M. Gandolfi, A. Tognazzi, D. Rocco, C. De Angelis, and L. Carletti, Phys. Rev. A **104**, 023524 (2021).

[28] L. Fagiani, M. Gandolfi, L. Carletti, C. de Angelis, J. Osmond, and M. Bollani, Micro Nano Eng. **19**, 100187 (2023).

[29] L. Fagiani, L. Bolzonello, J. Osmond, D. de Ceglia, N. van Hulst, M. Bollani, and M. A. Vincenti, Adv. Opt. Mater. **12**, 2301456 (2024).

[30] K. Sun, H. Jiang, D. A. Bykov, V. Van, U. Levy, Y. Cai, and Z. Han, Photon. Res. **10**, 1575 (2022).

[31] F. Wu, X. Qi, M. Qin, M. Luo, Y. Long, J. Wu, Y. Sun, H. Jiang, T. Liu, S. Xiao *et al.*, Phys. Rev. B **109**, 085436 (2024).

[32] A. Ndao, L. Hsu, W. Cai, J. Ha, J. Park, R. Contractor, Y. Lo, and B. Kanté, NanoPhoton. **9**, 1081 (2020).

[33] Z. Liu, Y. Xu, Y. Lin, J. Xiang, T. Feng, Q. Cao, J. Li, S. Lan, and J. Liu, Phys. Rev. Lett. **123**, 253901 (2019).

[34] A. Tognazzi, P. Franceschini, O. Sergaeva, L. Carletti, I. Alessandri, G. Finco, O. Takayama, R. Malureanu, A. V. Lavrinenko, A. C. Cino *et al.*, Adv. Photon. **5**, 066006 (2023).

[35] A. C. Overvig, S. Shrestha, and N. Yu, NanoPhoton. **7**, 1157 (2018).

[36] M. Moharam and T. K. Gaylord, J. Opt. Soc. Am. **71**, 811 (1981).

[37] J. A. Frantz, J. D. Myers, A. Clabeau, R. Y. Bekele, N. Hong, M. A. Vincenti, M. Gandolfi, and J. S. Sanghera, Opt. Mater. Express **13**, 3631 (2023).

[38] M. Gandolfi, L. Carletti, A. Tognazzi, A. C. Cino, C. De Angelis, and M. Guasoni, Opt. Express **31**, 31051 (2023).

[39] A. Tognazzi, M. Gandolfi, B. Li, G. Ambrosio, P. Franceschini, R. Camacho-Morales, A. C. Cino, C. Baratto, D. de Ceglia, D. Neshev *et al.*, Opt. Mater. Express **13**, 41 (2023).

[40] D. de Ceglia, M. Gandolfi, M. A. Vincenti, A. Tognazzi, P. Franceschini, A. C. Cino, G. Ambrosio, C. Baratto, B. Li, R. Camacho-Morales *et al.*, Opt. Lett. **48**, 2961 (2023).

[41] C. Baratto, M. Gandolfi, A. Tognazzi, P. Franceschini, G. Ambrosio, B. Li, R. C. Morales, D. de Ceglia, A. C. Cino, D. N. Neshev, and C. De Angelis, IEEE Sensors Letters **7**, 3502104 (2023).

[42] I. Ronneberger, W. Zhang, and R. Mazzarello, MRS Commun. **8**, 1018 (2018).

[43] M. Behrens, A. Lotnyk, J. W. Gerlach, M. Ehrhardt, P. Lorenz, and B. Rauschenbach, ACS Appl. Mater. Interfaces **11**, 41544 (2019).

[44] A. D. Cywar, Melting and crystallization of Si and $Ge_2Sb_2Te_5$ nanostructures, Ph.D. thesis, University of Connecticut Graduate School, 2016.

[45] M. Kuwahara, O. Suzuki, Y. Yamakawa, N. Taketoshi, T. Yagi, P. Fons, T. Fukaya, J. Tominaga, and T. Baba, Jpn. J. Appl. Phys. **46**, 3909 (2007).

[46] P. Zalden, K. S. Siegert, S. Rols, H. E. Fischer, F. Schlich, T. Hu, and M. Wuttig, Chem. Mater. **26**, 2307 (2014).